# Microwave-driven *i*SWAP-like gate for fixed-frequency superconducting transmon qutrits

Peng Xu [ORCID],[1,*] Qingli Jing,[2] Peng Zhao,[3,†] and Yang Yu [ORCID][3,4,5]

[1]*Institute of Quantum Information and Technology, Nanjing University of Posts and Telecommunications, Nanjing 210003, China*
[2]*Department of Optoelectronic Information of Science and Engineering, School of Science,*
*Jiangsu University of Science and Technology, Zhenjiang 212003, China*
[3]*National Laboratory of Solid State Microstructures, School of Physics, Nanjing University, Nanjing 210093, China*
[4]*Hefei National Laboratory, Hefei 230088, China*
[5]*Synergetic Innovation Center of Quantum Information and Quantum Physics,*
*University of Science and Technology of China, Hefei, Anhui 230026, China*

High-fidelity two-qubit gates are crucial for the scalability of superconducting quantum processors. While quantum information processing is typically based on qubits, qutrits (or qudits) provide a larger state space for quantum information storage and processing. In this study, we analyze a high-fidelity two-qutrit gate using microwave pulses on fixed-frequency superconducting transmon qutrits and show that a high-fidelity imaginary swap-like (*i*SWAP-like) gate can be achieved. Perturbation theory is employed to derive an effective interaction Hamiltonian, allowing us to estimate the gate time for the two-qutrit system. Moreover, by employing a microwave-activation scheme, we can realize a high-fidelity *i*SWAP-like gate on different excited states of the two qutrits. Our numerical results indicate that the proposed scheme can be readily extended to multiqutrit scenarios. Additionally, we investigate the impact of microwave pulse ramp time and qutrit relaxation on gate fidelity. The results demonstrate that, with a longer ramp time and the currently accessible qutrit relaxation time, the gate error remains sufficiently small. This proposed gate scheme enables the implementation of qutrit-qutrit entangling gates, providing a promising approach to realizing superconducting quantum computation.

## I. INTRODUCTION

To implement various quantum information tasks and achieve universal quantum computing [1,2], precise control of quantum systems is essential. Among the various quantum physical platforms, superconducting quantum circuit systems are considered one of the most promising candidates to realize quantum computers [2]. This promise was demonstrated by the success of a 53-qubit programmable superconducting quantum processor [3], preparation of 20-qubit entanglement [4], and simulation of quantum walk on a 62-qubit superconducting quantum information processor [5]. Quantum gates are crucial to the above advancements in quantum information processors, and any intricate quantum algorithm can be broken down into single-qubit, two-qubit, or multi-qubit operations [6]. In particular, a programmable or functional quantum information processor requires high-fidelity single- and two-qubit entangling gates such as controlled-Z (CZ) and *i*SWAP gates. However, realizing high-fidelity two-qubit entangling gates, which are essential for the realization of fault-tolerant quantum computing and quantum error correction, is still challenging.

In the past few decades, several schemes have been proposed to achieve high-fidelity quantum gate operations in superconducting quantum systems [7–12]. With significant progress made in the number and quality of superconducting qubits [13,14], quantum gate operations have been experimentally demonstrated with good performance. However, most of the gate schemes presented focused on the limitations of the lowest two states defined as a qubit. In contrast, quantum systems naturally possess multiple accessible quantum states that will improve the efficiency of quantum computing. For instance, qutrits (or qudits) can offer a three (or larger) quantum state space to store and process quantum information. Quantum information processors based on these larger state-space systems have shown significant advantages over qubit-based systems in quantum error correction [15–18] and quantum cryptography [19,20]. The available qudit-based operations can achieve higher encoding capabilities [21–26] and improve qubit readout [27,28]. Additionally, quantum control of high-dimensional states has been extensively exploited in superconducting transmon qutrits, such as in metrological algorithms [29], three-qutrit entanglement states [30], Toffoli gates [31], and more. In particular, the use of qutrit gates [32–34] could enhance the efficiency of circuit decompositions [35], and thus could pave an alternative way to extend quantum computing to three- or higher-level quantum systems.

In this work, we present a theoretical exploration of how to realize a two-qutrit entanglement gate based on a superconducting quantum system. The system consists of two fixed-frequency superconducting transmon qutrits coupled

*pengxu@njupt.edu.cn
†shangniguo@sina.com

to a common superconducting resonator. In contrast to frequency-tunable gate schemes, which require careful tuning of qubit frequencies to mitigate undesired dispersive interactions [36–43]. Here, we present a theoretical gate scheme for the implementation of a two-qutrit entanglement operation solely by microwave controls. This approach can potentially address the problems of frequency of crowding in the frequency-tunable gate schemes.

By combining virtual photon exchange with the resonator and microwave drives, an effective two qutrits interaction can be achieved. Therefore, depending on the drive parameters, the interaction can be used to implement two-qutrit operations. In this study, we focus on the two-qutrit $i$SWAP-like gate, defined in the second-excited states $\{|00\rangle, |20\rangle, |02\rangle, |22\rangle\}$ of the two-qutrit with the swap angle $\theta = \pi/2$ and the conditional phase $\phi$ of state $|22\rangle$. With the defined basis states, the iSWAP-like gate can be written as [39]

$$
i\text{SWAP}_{\text{like}} = \begin{bmatrix} 1 & 0 & 0 & 0 \\ 0 & 0 & -i & 0 \\ 0 & -i & 0 & 0 \\ 0 & 0 & 0 & e^{-i\phi} \end{bmatrix}. \tag{1}
$$

Our proposal demonstrates a high-fidelity $i$SWAP-like gate by controlling microwave pulse parameters. To gain further insight into the gate operation, we performed a perturbative analysis and derived an effective Hamiltonian for the two transmon qutrits system. We show that a two-qutrit $i$SWAP-like gate can be completed in 280 ns (including the pulse ramp time) with an average fidelity exceeding 99.87%. By prolonging the pulse ramp time, an intrinsic gate fidelity of 99.9% (or higher) can be achieved in 310 ns. Additionally, logical operations on different excited states of qutrits, such as population swapping between states $|20\rangle$ and $|01\rangle$, may potentially simplify intricate quantum algorithms. We further demonstrate that the high-fidelity $i$SWAP-like gate defined in different excited states $|20\rangle$ and $|01\rangle$ of the two qutrits can be implemented by applying a single microwave pulse to activate the qutrit.

The paper is organized as follows. In Sec. II, we describe the superconducting quantum model and present a simplified analytic treatment. In Sec. III, we give a detailed discussion of how to realize the $i$SWAP-like gate and present the numerical results of the system dynamics during the gate operation. In Sec. IV, we analyze the case of this gate scheme for different excited states of the two transmon qutrits. In Sec. V, we discuss the average gate fidelity versus different ramp times of microwave pulses and the reduction due to relaxation. Finally, we conclude in Sec. VI. Furthermore, in Appendix A, we give out the analytical effective coupling strength through the perturbation theory. In Appendix B, we explore the possibilities of an arbitrary two-qutrit $i$SWAP-like gate by expanding our investigation to encompass the multi-qutrit scenario. Additionally, Appendix C provides a comprehensive discussion on leakage errors for the two-qutrit gate operation.

## II. MODEL OF SUPERCONDUCTING TRANSMON QUTRITS

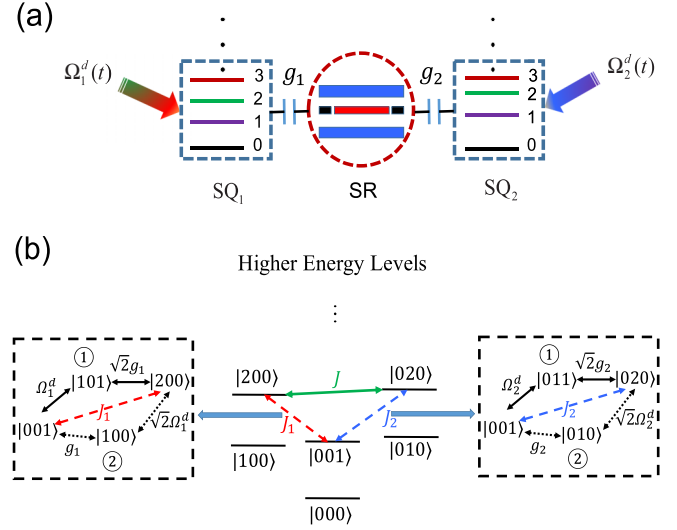In this section, we will introduce the architecture of the superconducting quantum circuit. The system, as shown in



FIG. 1. (a) The proposed superconducting quantum circuit consists of two superconducting qutrits, $SQ_j$, which are capacitively coupled to a superconducting resonator. The *ladder*-type levels of qutrit-$j$ comprise four states and the computational states are defined in the basis states $|0\rangle, |2\rangle$ of qutrits. The $SQ_j$ transition frequencies $\omega_j$ (the transition frequency of the lowest two energy levels), the anharmonicity $\alpha_j$, and the qutrit-resonator coupling strength $g_j$, are fixed. (b) The energy-level diagram of the system shows that microwave pulses $\Omega_1^d(t)$ and $\Omega_2^d(t)$, performed on the qutrits could induce effective interactions $|200\rangle \leftrightarrow |001\rangle$ and $|020\rangle \leftrightarrow |001\rangle$, respectively. The black-dashed box on the left (right) illustrates that the effective interaction strength $J_1$ ($J_2$) between the states $|200\rangle \leftrightarrow |001\rangle$ ($|020\rangle \leftrightarrow |001\rangle$) could be obtained through two evolution paths: ① $|200\rangle \leftrightarrow |101\rangle \leftrightarrow |001\rangle$ ($|020\rangle \leftrightarrow |011\rangle \leftrightarrow |001\rangle$) indicated by solid double-arrows and ② $|200\rangle \leftrightarrow |100\rangle \leftrightarrow |001\rangle$ ($|020\rangle \leftrightarrow |010\rangle \leftrightarrow |001\rangle$) presented by dotted double-arrows. By exchanging the virtual photon with the resonator, one can realize effective interactions between $|200\rangle$ and $|020\rangle$ with the strength $J$.

Fig. 1(a), consists of two fixed-frequency superconducting transmon qutrits coupled to a superconducting resonator (SR). Due to the larger state space of the superconducting qutrits, the higher-energy levels have a nonnegligible effect, so the closest higher-energy state $|3\rangle$ is also considered in the following discussions. As depicted in Fig. 1(a), both qutrits are truncated to four levels (i.e., $|0\rangle, |1\rangle, |2\rangle$, and $|3\rangle$), the qutrits can be modeled as a four-level anharmonic oscillator with a negative anharmonicity. The resonator, on the other hand, could be considered a simple four-level harmonic oscillator. The transmon qutrits are capacitively coupled to the most relevant single mode of the resonator, and the system can be modeled by the Hamiltonian (hereafter $\hbar = 1$)

$$
H_s = \sum_j \left( w_j q_j^\dagger q_j + \frac{\alpha_j}{2} q_j^\dagger q_j^\dagger q_j q_j \right) + w_r c^\dagger c
$$
$$
+ \sum_j g_j (q_j^\dagger + q_j)(c^\dagger + c), \tag{2}
$$

where subscript $j = 1, 2$ represents the transmon qutrits labeled as $SQ_j$ with bare frequency $\omega_j$ (the $|0\rangle \rightarrow |1\rangle$ transition frequency of qutrit-$j$) and anharmonicity $\alpha_j$. The $q_j$

($q_j^\dagger$) is the associated annihilation (creation) operator for $SQ_j$. The $c$ ($c^\dagger$) denotes the annihilation (creation) operator for the resonator mode with a bare frequency of $w_r$, and $g_j$ is the coupling strength between $SQ_j$ and $SR$. Throughout the paper, we consider the full system state $|SQ_1, SQ_2, SR\rangle$, which corresponds to the states of qutrit-1, qutrit-2, and the resonator, respectively. When confined to the qutrit subspace, we use the notation $|SQ_1, SQ_2\rangle$.

For the fixed frequencies of the qutrits and the coupling strength between the qutrits and resonator, perfect population swaps between the specific states of the qutrits can be challenging to achieve due to the complex system dynamics. However, by exchanging the virtual photon with the resonator which acts as an intermediary bus, an effective interaction between the two qubits can be obtained [44–46]. In this study, to realize the effective interaction between the second excited states of the two qutrits, we apply two external microwave pulses $\Omega_1^d(t)$ and $\Omega_2^d(t)$ to activate the qutrits $SQ_1$ and $SQ_2$, respectively. The Hamiltonian for the microwave-activated part is described by

$$H_d = \sum_j \Omega_j \cos(\omega_j^d t)(q_j^\dagger + q_j).\tag{3}$$

The pulse amplitude is denoted as $\Omega_j$, while the pulse frequency is represented by $\omega_j^d$. For simplicity, the initial phase of the pulse is set to 0. When the pulse frequencies are set as $\omega_1^d \approx 2\omega_1 + \alpha_1 - \omega_r$ and $\omega_2^d \approx 2\omega_2 + \alpha_2 - \omega_r$, we can obtain the effective interactions between the states $|200\rangle$ and $|020\rangle$, as depicted in Fig. 1(b). There exist 12 evolution paths connecting the states $|200\rangle$ and $|020\rangle$, facilitated by intermediate states $|001\rangle$, $|111\rangle$, and $|110\rangle$ (refer to Appendix A for a comprehensive elucidation of these paths) [47].

Here, for example, we consider the contribution associated with the intermediate state $|001\rangle$ to illustrate the main physics behind the effective coupling between states $|200\rangle$ and $|020\rangle$. As illustrated in the left black-dashed box of Fig. 1(b), when the microwave pulse $\Omega_1^d(t)$ is driven on $SQ_1$, it activates the effective interaction $|200\rangle \leftrightarrow |001\rangle$ through two evolution paths: $|200\rangle \leftrightarrow |101\rangle \leftrightarrow |001\rangle$ and $|200\rangle \leftrightarrow |100\rangle \leftrightarrow |001\rangle$. Assuming that the qutrit interacts with the resonator and microwave pulse in the dispersive regime [44–46], where the qutrit-resonator and qutrit-pulse detunings are far larger than their coupling strength, the effective coupling strength $J_1$ between $|200\rangle$ and $|001\rangle$ for the above two evolution paths can be obtained according to the perturbation theory [47–49].

Likewise, by applying the microwave pulse $\Omega_2^d(t)$ on $SQ_2$, we can also derive the effective interaction strength $J_2$ between the $|020\rangle \leftrightarrow |001\rangle$ interaction via two evolution paths, namely, $|020\rangle \leftrightarrow |011\rangle \leftrightarrow |001\rangle$ and $|020\rangle \leftrightarrow |010\rangle \leftrightarrow |001\rangle$, as illustrated in the right black-dotted box in Fig. 1(b). The effective coupling strength $J_j$ ($j = 1, 2$) can be approximately expressed as [48]

$$J_j = \frac{\sqrt{2}g_j\Omega_j}{4}\left(\frac{1}{\omega_j^d - \omega_j} - \frac{1}{\omega_r - (\omega_j + \alpha_j)}\right)$$
$$+ \frac{\sqrt{2}g_j\Omega_j}{4}\left(\frac{1}{\omega_r - \omega_j} - \frac{1}{\omega_j^d - (\omega_j + \alpha_j)}\right).\tag{4}$$

In Eq. (4), the first line corresponds to the evolution path ① represented by the solid double-arrows, while the second line corresponds to the evolution path ② denoted by the dotted double-arrows, as shown in the left and right black-dashed box of Fig. 1(b). As a result, the above system can be reduced to two effective two-level systems that interact with each other through the resonator. If we assume that the reduced two-level qutrit is still detuned from the resonator, such that $|2\omega_j + \alpha_j - 2\omega_r| \gg J_j$, we can exchange virtual photons with the resonator to realize effective interactions between the states $|200\rangle$ and $|020\rangle$. Under the dispersive condition, the resonator mode can be eliminated adiabatically [14], giving rise to the following effective Hamiltonian:

$$H_I = J_{001}(|200\rangle\langle020| + |020\rangle\langle200|),\tag{5}$$

with the coupling strength $J_{001} = \frac{J_1 J_2}{2}\left(\frac{1}{\Delta_1'} + \frac{1}{\Delta_2'}\right)$. The detuning term in the computational basis is given by $\Delta_j' \approx 2\omega_j + \alpha_j - \omega_r - \omega_j^d$, taking into account the detuning of both qutrits from the resonator and the driven pulse. As in Appendix A, by considering all these evolution paths and employing the fourth-order perturbation theory, the effective coupling strength, denoted as $J$, for states $|200\rangle$, $|020\rangle$ is obtained. Then, the gate speed for the *i*SWAP-like gate can be estimated.

Moreover, the intrinsic properties of the quantum systems also play a crucial role in achieving high-fidelity quantum gate operations. For instance, weak anharmonicity in transmons can induce a static *ZZ* coupling [42], leading to additional phases that can affect gate fidelity. Therefore, it is imperative to minimize this residual interaction. To this end, we set the anharmonicities of transmons to $\alpha_j/2\pi = -300$ MHz, the resonator frequency $\omega_r/2\pi = 5.3$ GHz, and the coupling strength $g_j/2\pi = 80$ MHz. Next, we investigate the *ZZ* coupling strength in the first and second excited states of the qutrits as a function of their frequencies, which are given by the following expressions [42]

$$\zeta_1 = (E_{11} - E_{01}) - (E_{10} - E_{00}),$$
$$\zeta_2 = (E_{22} - E_{02}) - (E_{20} - E_{00}).\tag{6}$$

Here, $\zeta_1$ and $\zeta_2$ represent the first and second excited states of the system, respectively. The $E_{mn}$ denotes the eigenenergy of the Hamiltonian $H_s$ for the system, with the eigenstate $|\widetilde{mn}\rangle$ confined to the qutrit subspace that is adiabatically connected to the bare state $|mn0\rangle$ [50].

We numerically calculate the *ZZ* coupling strength as a function of the transmon frequency $\omega_j$ and present the results in Fig. 2. For the first excited state, the static *ZZ* coupling strength can be suppressed to less than 50 kHz, as shown in Fig. 2(a). Similarly, the *ZZ* coupling strength in the second excited state can be suppressed to as small as 50 kHz, as shown in Fig. 2(b). We can observe from Fig. 2 that chosen special values of the qutrit frequencies can help minimize the residual *ZZ* interaction. However, due to the original fixed coupling strength, the qutrit frequency parameters cannot be arbitrarily chosen to obtain an affable gate time. For example, selecting the frequencies $\omega_1/2\pi = 4.5$ GHz and $\omega_2/2\pi = 6.5$ GHz, which induce ZZ interaction $-16.2$ kHz ($-52.4$ kHz) in the first (second) excited state, results in a minimum *i*SWAP-like gate time of approximately
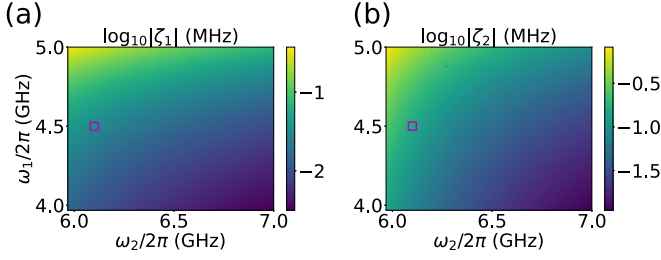
FIG. 2. Numerical results show the ZZ coupling strength in the first and second excited states. Panel (a) displays the $\log_{10}|\zeta_1|$ coupling strength in the first-excited states as a function of the two-qutrit frequencies $\omega_1$ and $\omega_2$. Panel (b) shows the ZZ coupling $\log_{10}|\zeta_2|$ versus $\omega_1$ and $\omega_2$ in the second-excited states of the two-qutrit. The anharmonicities $\alpha_j/2\pi$ are set to $-300$ MHz, the coupling strengths $g_j/2\pi$ to 80 MHz, and the resonator frequency $\omega_r/2\pi$ to 5.3 GHz. The magenta square in both (a) and (b) represents the selected frequencies of the two-qutrit discussed in Sec. III.

$\sim 300$ ns using the presented method (details discussed in Sec. III). To reduce the gate operation time, we increase the coupling strength to $g_2/2\pi = 120$ MHz, resulting in a gate time of $\sim 220$ ns. However, this increases the ZZ interaction strength to $-36.7$ kHz ($-114.7$ kHz) in the first (second) excited state. Hence, there is a trade-off between the gate time and additional phases induced by the system parameters. According to the practical parameters used in the literature [13,25,48], we choose the values of qutrits frequencies $\omega_1/2\pi = 4.5$ GHz and $\omega_2/2\pi = 6.1$ GHz, shown by the magenta-square in Fig. 2, to make the system work in the dispersive regime and suppress the effect of ZZ coupling strength as much as possible. In the following, with system parameters presented in Table I, we discuss how to realize the two-qutrit $i$SWAP-like gate.

## III. REALIZATION OF $i$SWAP-LIKE GATE

The $i$SWAP-like gate operation described in Eq. (1) enables high-fidelity population swapping between the second excited states of the two qutrits. We consider that the system parameters are fixed once the superconducting transmon qutrits and resonator are fabricated. To prevent resonant interactions between the qutrits and the resonator, it is necessary to increase the detuning $\Delta'_j$ between them. In our study, we chose to set this detuning to approximately 40 MHz. Given the fixed system parameters values, we consider the microwave pulses defined by Eq. (3) with a constant pulse amplitude $\Omega_j$ and assume that the frequency $\omega_1^d$ of the pulse applied to $SQ_1$ is fixed for simplicity. To achieve an accurate $i$SWAP-like gate between the two qutrits, we need to determine the precise value of the frequency $w_2^d$ for the pulse applied to
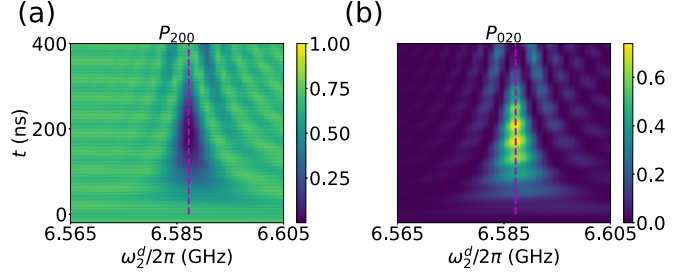


FIG. 3. The populations of the initial state $|200\rangle$ versus pulse frequency $\omega_2^d$ and evolution time $t$ under the full Hamiltonian ($H_s + H_d$) are shown in (a), while (b) displays the populations for the swap state $|020\rangle$ after the evolution. The applied microwave-driven pulse is described in Eq. (3), with a frequency of $\omega_1^d/2\pi \simeq 3.348$ GHz, $\Omega_{1(2)}^0/2\pi = 200$ MHz, and $\Delta'_{1(2)}/2\pi = 40$ MHz. The vertical cuts in (a) and (b) represent the populations of states $|200\rangle$ and $|020\rangle$ with the chosen value of pulse frequency $\omega_2^d/2\pi \simeq 6.587$ GHz. The system parameters are listed in Table I.

$SQ_2$. In the following, we use the estimated frequency value $\omega_2^d \approx 2\omega_2 + \alpha_2 - \omega_r - \Delta'_2$ as a reference to obtain the good microwave pulse frequency value.

To determine the precise value of the pulse frequency $\omega_2^d$ required for the $i$SWAP-like gate operation, we perform numerical calculations of the populations $P_{200}$ and $P_{020}$ (corresponding to the states $|200\rangle$ and $|020\rangle$, respectively) as a function of $\omega_2^d$ and time $t$ with the full system initialized in state $|200\rangle$, microwave pulse amplitude $\Omega_{1(2)}/2\pi = 200$ MHz, driving frequency $\omega_1^d/2\pi$ of approximately 3.348 GHz, and qutrits-resonator detuning $\Delta'_{1(2)}/2\pi = 40$ MHz. As shown in Fig. 3, by combining the valley and peak populations of $|200\rangle$ and $|020\rangle$, we find that a proper swap operation is achievable at a specific value of the pulse frequency $\omega_2^d$. We select the frequency $\omega_2^d/2\pi \simeq 6.587$ GHz, indicated by the vertical magenta-dashed lines in Fig. 3, which is close to the estimated value of 6.585 GHz discussed earlier. Moreover, one can find that an almost completed population swap between states $|200\rangle$ and $|020\rangle$ can be successfully executed within $\sim 200$ ns, which agrees well with an estimation based on the effective coupling strength of $J/2\pi \approx 1.217$ MHz, as deduced from Eq. (A4).

In the following, we analyze the dynamics using the optimal pulse frequency $\omega_2^d/2\pi \simeq 6.587$ GHz. With the initial state $|200\rangle$ and the microwave pulses defined in Eq. (3), we plot the system evolution under the full Hamiltonian ($H_s + H_d$) in Fig. 4(a), which corresponds to the vertical magenta-dashed cuts in Figs. 3(a) and 3(b). However, the plot shows that the population swap between states $|200\rangle$ and $|020\rangle$ is not achieved completely. This is because the applied microwave pulses $\Omega_{1(2)}^d(t)$ defined in Eq. (3) are square pulses. To achieve the two-qutrit $i$SWAP-like gate, we need to consider the microwave pulse shape with a Gaussian form

TABLE I. System parameters for the two-qutrit $i$SWAP-like gate.

| | Bare frequency (GHz) | Anharmonicity (MHz) | Coupling (MHz) |
|---|---|---|---|
| $SQ_1$ | $\omega_1/2\pi = 4.5$ | $\alpha_1/2\pi = -300$ | $g_1/2\pi = 80$ |
| $SR$ | $\omega_r/2\pi = 5.3$ | $\alpha_c/2\pi = 0$ | $g_2/2\pi = 80$ |
| $SQ_2$ | $\omega_2/2\pi = 6.1$ | $\alpha_2/2\pi = -300$ | |

$$G_j^d(t) = \begin{cases} \frac{e^{-(t-t_r)^2/(2\delta^2)} - e^{-t_r^2/(2\delta^2)}}{1 - e^{-t_r^2/(2\delta^2)}}, & t \leqslant t_r, \\ 1, & t_r < t < t_p - t_r, \\ \frac{e^{-(t-(t_p-t_r))^2/(2\delta^2)} - e^{-t_r^2/(2\delta^2)}}{1 - e^{-t_r^2/(2\delta^2)}}, & t - t_r \leqslant t \leqslant t_p, \\ 0, & \text{others}, \end{cases} \tag{7}$$
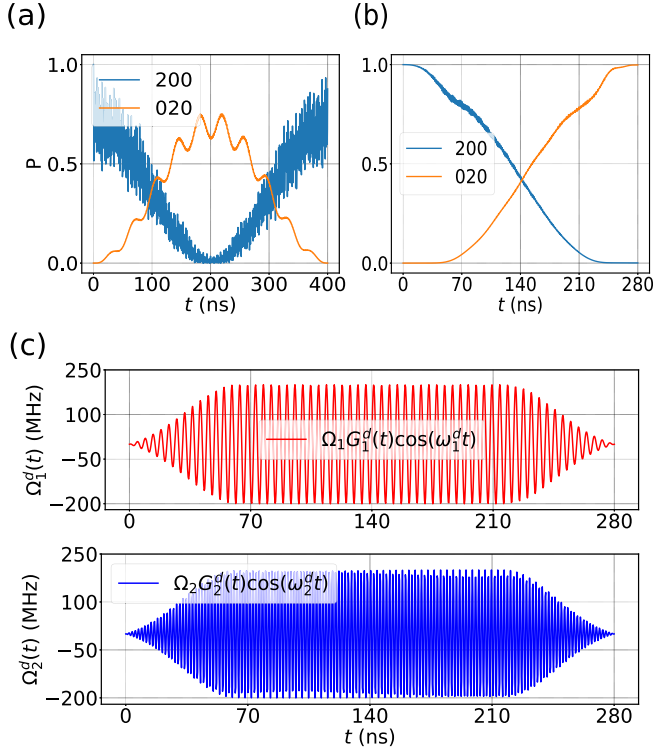
FIG. 4. System dynamics during the gate operation and the corresponding microwave pulses. (a) The populations of states $|200\rangle$ and $|020\rangle$ correspond to the vertical cuts in Fig. 3, with applied microwave pulses defined in Eq. (3) and the pulse parameters $\Omega_{1(2)}^0/2\pi = 200$ MHz, $\omega_1^d/2\pi \simeq 3.348$ GHz, and $\omega_2^d/2\pi \simeq 6.587$ GHz. (b) Populations of the states $|200\rangle$ and $|020\rangle$ during the $i$SWAP-like gate operation, with applied pulse drivings performed on the qutrit given in Eq. (8). These pulses have the parameters $\Omega_{1(2)}/2\pi = 200$ MHz, $\delta = 30$ ns, $t_r = 2.1\delta$, $t_p = 280$ ns, $\omega_1^d/2\pi \simeq 3.348$ GHz, and $\omega_2^d/2\pi \simeq 6.587$ GHz. The other system parameters are presented in Table I. Considering the pulse shape, the drive microwaves $\Omega_1^d(t)$ (red line) performed on $SQ_1$ and $\Omega_2^d(t)$ (blue line) performed on the $SQ_2$ are shown in the top and bottom of (c).

where the microwave pulse is shape-controllable and is confined by the ramp time $t_r$, the variance $\delta$ of the Gaussian pulse, and the total time $t_p$. It is worth noting that there are subtle relationships among the pulse parameters $t_r$, $\delta$, and $t_p$. For simplicity, we assume that the ramp time is related to the variance by $t_r = 2.1\delta$. Consequently, we redefine the shape-controllable microwave pulse as

$$\Omega_j^d(t) = \Omega_j G_j^d(t)\cos\left(\omega_j^d t\right). \tag{8}$$

We begin by considering the Gaussian pulse with ramp-up and ramp-down times of $t_r$ each. With the given system parameters and chosen pulse frequencies, we then investigate the system dynamics further by varying $t_p$ for each value of $\delta$. To do this, we select $\delta = 30$ ns and $t_g = 280$ ns which is chosen from the time region shown in Fig. 3. Using these parameters, we investigate the dynamics during the implementation of an $i$SWAP-like gate operation, as displayed in Fig. 4(b). Our results show that by considering the pulse shape, a complete swap can be achieved. The slower speed (larger $\delta$ with ramp time $t_r = 2.1\delta$) can prevent leakage to the noncomputational

TABLE II. System parameters for the two-qutrit $i$SWAP-like gate defined in different excited states.

| | Bare frequency (GHz) | Anharmonicity (MHz) | Coupling (MHz) |
|---|---|---|---|
| $SQ_1$ | $\omega_1/2\pi = 4.9$ | $\alpha_1/2\pi = -250$ | $g_1/2\pi = 120$ |
| $SR$ | $\omega_r/2\pi = 5.3$ | $\alpha_c/2\pi = 0$ | $g_2/2\pi = 120$ |
| $SQ_2$ | $\omega_2/2\pi = 5.7$ | $\alpha_2/2\pi = -240$ | |

states. The selection of $\delta$ value will be discussed in Sec. V. Considering the pulse shape, we demonstrate the microwave pulses $\Omega_1^d(t)$ and $\Omega_2^d(t)$ correspond to the top and bottom of Fig. 4(c), respectively. This further emphasizes the importance of the pulse shape in achieving a high-fidelity $i$SWAP-like gate. Additionally, one can first fix the frequency $\omega_2^d$ and then find the frequency value of $\omega_1^d$ following the above discussions. Furthermore, through the presented gate scheme, we verify that one can also find the exact parameter values of microwave pulses to realize the high-fidelity $i$SWAP-like gate defined in different excited states of the two qutrits.

## IV. ANALYSIS OF THE $i$SWAP-LIKE GATE FOR DIFFERENT EXCITED STATES OF THE TWO-QUTRIT

The superconducting quantum system offers optimism for large-scale and complex quantum computing, thanks to its ability to perform quantum operations on diverse energy levels. As shown in Fig. 1, the transmon qutrits possess multiple energy levels, and the presented scheme can also realize the $i$SWAP-like gate between different excited states of the two qutrits. For instance, we assume that the computational subspace is $\{|00\rangle, |20\rangle, |01\rangle, |21\rangle\}$, where the state $|21\rangle$ denotes the $SQ_1$ in the second excited state and $SQ_2$ in the first excited state. Based on the above discussions, the $|20\rangle \rightarrow |01\rangle$ transition can be realized by applying only one microwave pulse on $SQ_1$. To illustrate the generality of the gate scheme, we apply different qutrit parameter values displayed in Table II. In this case, a microwave pulse drive is only applied to qutrit-1.

Based on the analysis above, we begin by applying the microwave pulse defined in Eq. (3) with the given parameters $\Omega_1/2\pi = 200$ MHz and $\Delta'_{1(2)}/2\pi = 40$ MHz. We then numerically calculate the populations of states $|200\rangle$ and $|010\rangle$ as a function of $\omega_1^d$ and time $t$, shown in Figs. 5(a) and 5(b). By inspecting the system dynamics, one can obtain the drive parameters for implementing an $i$SWAP-like gate. To investigate the dynamics without considering the pulse shape, we cut the three-dimensional Figs. 5(a) and 5(b) at the microwave pulse frequency point $\omega_1^d/2\pi \simeq 3.758$ GHz and plotted the change of the populations. From Fig. 5(c), we observe that the population swap cannot be completed without considering the pulse shape. However, by using the microwave pulse defined in Eq. (8) and initializing the system in the state $|200\rangle$, we simulate the system dynamics with the pulse frequency value $\omega_1^d/2\pi \simeq 3.758$ GHz and the other pulse parameters $\Omega_1/2\pi = 200$ MHz, $\delta = 30$ ns, $t_r = 2.1\delta$, and $t_p = 287$ ns, as shown in Fig. 5(d). We find that the perfect population swap between $|200\rangle$ and $|010\rangle$ is achieved. While the system parameters tabulated in Table II may indicate that the system does not work in the dispersive regime, where the detuning
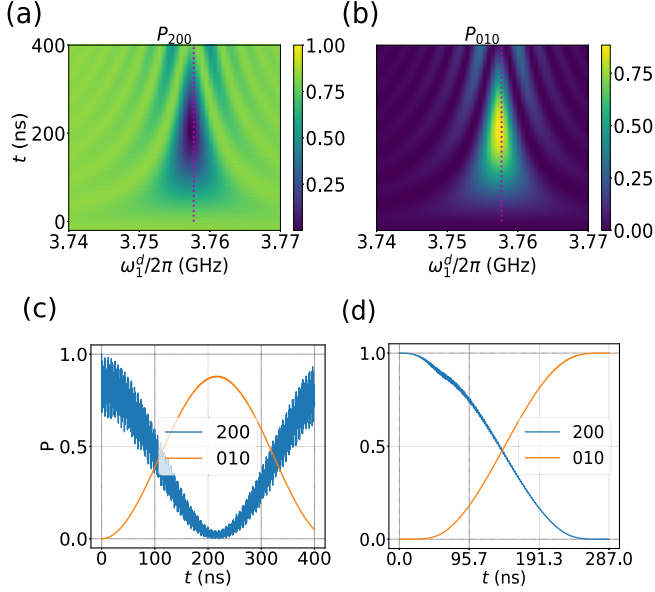
FIG. 5. The $i$SWAP-like gate for different excited states of two qutrits. Populations of quantum state (a) $|200\rangle$ and (b) $|010\rangle$ are shown as a function of microwave pulse frequency and time. (c) Dynamics of state transitions $|200\rangle \rightarrow |010\rangle$ with microwave pulse frequency $\omega_1^d/2\pi \simeq 3.758$ GHz without considering the pulse shape. The populations of states $|200\rangle$ and $|010\rangle$ correspond to the magenta-dotted vertical cuts in (a), (b), respectively. (d) The dynamic evolution of quantum states $|200\rangle$ and $|010\rangle$ with the applied microwave pulse defined in Eq. (8) and parameters $\Omega_1^0/2\pi = 200$ MHz, $\delta = 30$ ns, $t_r = 2.1\delta$, $t_p = 287$ ns, $\omega_1^d/2\pi \simeq 3.758$ GHz. The parameter values for qutrits and resonator are provided in Table II.

is much larger than the interaction strength, our gate scheme demonstrates that the high-fidelity $i$SWAP-like gate can still be achieved.

## V. DISCUSSION OF FIDELITY

We now aim to quantify the fidelity of the $i$SWAP-like gate for the two-qutrit system. The unitary operation governing the $i$SWAP-like gate can be succinctly expounded utilizing a general two-qubit formalism [51] (here the basis is $\{|00\rangle, |20\rangle, |02\rangle, |22\rangle\}$)

$$U = e^{-i(IZ-ZI)\varphi_1/4} e^{-i(XX+YY)\theta/2} e^{-i(ZZ)\phi/4}$$
$$\times e^{-i(IZ-ZI)\varphi_2/4} e^{-i(IZ+ZI)\varphi_3/4}, \quad (9)$$

where specifying the swap angle $\theta$, conditional phase $\phi$, and the single-qubit phases $\varphi_{1,2,3}$. Assuming the ideal swap with $\theta = \pi$, we quantify the performance of the implemented $i$SWAP-like gate using the state-average gate fidelity metric defined in [52]

$$F(\varphi_1, \phi, \varphi_2, \varphi_3) = \frac{[\text{Tr}(U_{\text{real}}^\dagger U_{\text{real}}) + |\text{Tr}(U^\dagger U_{\text{real}})|^2]}{20}, \quad (10)$$

where $U_{\text{real}}$ is the actual evolution operator projected to the computational subspace (without considering the effect of decoherence). This is evaluated based on the system dynamics under the full Hamiltonian. For the single-qubit phases $\varphi_{1,2,3}$, one can implement the single-qubit phase operations before and after the $i$SWAP-like gate to correct the local phases

of the single qubits [53–55]. For the two-qutrit $i$SWAP-like gate, we optimized the single-qubit phases $\varphi_1 \simeq 0.222$ rad, $\varphi_2 \simeq 0.422$ rad, $\varphi_3 \simeq 0.020$ rad, and conditional phase $\phi \simeq 1.366$ rad to obtain a numerically calculated average gate fidelity $F$ of 99.87%. For different excited states of two qutrits, the average fidelity of the $i$SWAP-like gate between states $|200\rangle$ and $|010\rangle$ can reach $F = 99.99\%$ with the single-qubit phases $\varphi_1 \simeq 0.536$ rad, $\varphi_2 \simeq -0.827$ rad, $\varphi_3 \simeq 0.334$ rad, and conditional phase $\phi \simeq 2.418$ rad.

Generally, achieving high-fidelity microwave-activated quantum gates typically requires longer pulse ramp time as this can mitigate off-resonant errors [56–58] during the gate operation. This is because there exists a delicate balance between the control error and ramp time. To investigate the effect of pulse ramp time on the isolated two-qutrit $i$SWAP-like gate discussed in Sec. III, we numerically calculated the gate error with different ramp times ($t_r = 2.1\delta$) of the driven pulse, as shown in Fig. 6(a) (with the corresponding pulse parameter $t_p$ shown in the inset). Our results indicate that the gate error decreases as the pulse ramp time increases. To be more explicit, for a gate pulse with a shorter ramp time, the off-resonant interactions can induce control error and population leakage (see Appendix C for more detail). To mitigate off-resonant errors, a longer ramp time is generally preferred. Indeed, our simulations suggest that the gate fidelity can be improved to 99.9% or higher by increasing the ramp time.

It is widely and generally known that to achieve high-fidelity gate operations, leakage errors can be a dominant error source and thus should be mitigated. The leakage errors occur when the quantum system leaks out of a defined computational subspace to occupy a noncomputational subspace. The subspace containing the system's energy levels where ideal dynamics take place is denoted as the computational subspace, represented by $V_1$ and characterized by a dimensionality of $d_1$. Additionally, we define the leakage subspace, denoted as $V_2$, which encompasses the $d_2$-dimensional space. Consequently, the overall state space of the system can be described as a direct sum $V = V_1 \oplus V_2$ with dimensions $(d_1 + d_2)$. For a quantum system in state $\rho$, the leakage can be defined as [59]

$$L(\rho) = Tr[A_2\rho] = 1 - \text{Tr}[A_1\rho], \quad (11)$$

where $A_1$ and $A_2$ denote the projectors onto the subspaces $V_1$ and $V_2$, respectively.

In this context, we delve into the topic of leakage errors, which pertain to the populations that have leaked from the computational subspace. Leakage errors are defined as follows [59]:

$$L_\varepsilon = \int dV_1 L(|V_1\rangle\langle V_1|) = L\left(\frac{V_1}{d_1}\right), \quad (12)$$

where the integrals are evaluated over all states within the computational subspace $|V_1\rangle$. Based on Eq. (12), we perform numerical calculations to determine the leakage errors, and the corresponding results are presented in Fig. 6(b). Our findings reveal that longer ramp times lead to a decrease in the magnitude of leakage errors. By conducting numerical simulations and assessing the populations that leaked into noncomputational subspaces, we identify that the primary contributors to the leakage errors were the states $|200\rangle$, $|020\rangle$, and $|220\rangle$. Notably, for the state $|000\rangle$, we observe that the leakage errors
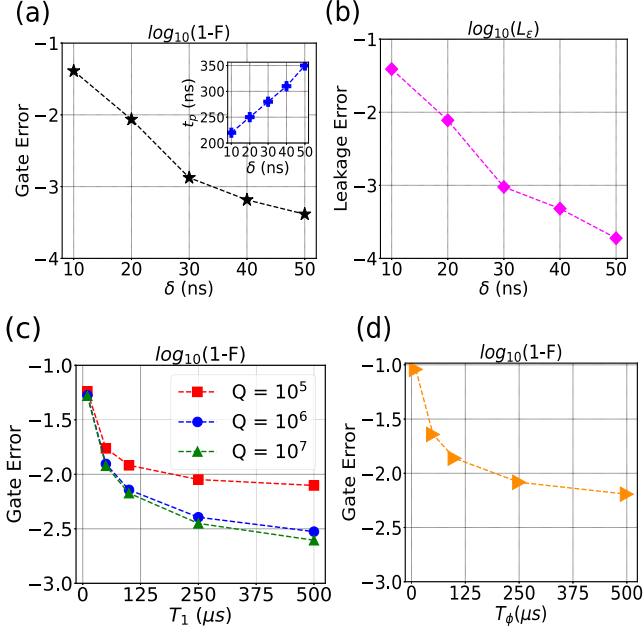
FIG. 6. Analysis of gate error for the two-qutrit *i*SWAP-like gate. (a) Gate error for different pulse ramp times, $t_r = 2.1\delta$. The inset shows the corresponding microwave pulse parameter $t_p = (220, 250, 280, 310, 340)$ ns for different $\delta$. The longer ramp time ensures a higher fidelity of the *i*SWAP-like gate. (b) Leakage errors after the two-qutrit *i*SWAP-like gate operation. The results demonstrate that extending the ramp time significantly reduces leakage errors. (c) Change in gate error due to qutrit relaxation with the parameter $\delta = 30$ ns, corresponding to the third point in (a). Here, we assume that all transmon qutrits have identical relaxation rates. The resonator decay rate is fixed as $\kappa = \omega_r/Q$, with three different quality factor values assumed for the qutrits having identical relaxation times. The results show that the gate error can be suppressed below 0.003 when the qutrit coherence time is over 500 μs. When the resonator quality factor surpasses $10^6$, the reduction in gate fidelity becomes smaller. (d) The gate error as a function of the qutrits dephasing time $T_\phi$ (white noise). We consider two transmon qutrits to have the same dephasing time. Here, the resonator quality factor is $Q = 10^6$, qutrits' relaxation time is 200 μs, and $\delta = 30$ ns corresponds to the third data point depicted in (a).

could be minimized to below $10^{-5}$ all the time. In contrast, for the states $|200\rangle$ (or $|020\rangle$) and $|220\rangle$, the leakage errors are 0.06 and 0.04 with $\delta = 10$ ns, respectively. However, by increasing the ramp time to $\delta = 40$ ns, the leakage errors associated with $|200\rangle$ (or $|020\rangle$) and $|220\rangle$ diminish to values below $10^{-3}$. A comprehensive analysis of the leakage errors is provided in Appendix C.

The above analysis of gate performance was conducted without considering the system decoherence process. We will now examine the effects of relaxation on gate performance, which arise from two main sources: the transmon qutrits and the resonator relaxation processes. Currently, experimental superconducting resonators with internal quality factors above $10^6$ have been demonstrated [60–62], providing sufficient coherence times for present technology. Therefore, we only consider three different values of the resonator's quality factor. Taking the qutrits' decoherence process into account, we can

express the master equation as [63]

$$\dot{\rho}(t) = -i[H_s + H_d, \rho] + \sum_{k=j,r} \mathcal{D}[C_k]\rho, \tag{13}$$

with $\mathcal{D}[C]\rho = C\rho C^\dagger - (C^\dagger C\rho + \rho C^\dagger C)/2$ and $C_{j,r} = \{\sqrt{1/T_j}q_j, \sqrt{\kappa}c, \sqrt{2/T_{p_j}}q_j^\dagger q_j \}$. Here, $T_j$ and $T_{\phi_j}$ signify, respectively, the relaxation and dephasing times of qutrit-$j$, while $\kappa = \omega_r/Q$ represents the resonator decay rate, where $Q$ stands for the quality factor of the resonator.

Based on Eqs. (10) and (13), Fig. 6(c) shows the gate error as a function of the relaxation time $T_1$ of the qutrits with three different values of the resonator quality factor. With the consideration of the relaxation process, the gate error will increase to 0.053. Meanwhile, an *i*SWAP-like gate with an error below 0.01 can be achieved with the relaxation time exceeding 100 μs. Compared to the qutrits relaxation process, the gate error caused by the resonator decay process can be omitted when the resonator quality factor reaches $10^6$ or higher. Moreover, in Fig. 6(d), we also show the gate error as a function of dephasing time (white noise) by assuming equal dephasing rates for the qutrits ($T_{\phi_{1,2}} = T_\phi$). Given the state-of-the-art coherence time of transmon [64,65], we expect that the *i*SWAP-like with the gate fidelity above 99% could be achieved.

## VI. CONCLUSION

In this study, we propose a microwave-driven scheme for implementing an *i*SWAP-like gate using fixed-frequency superconducting transmon qutrits. The qutrits are coupled to a common resonator with a constant coupling strength. By using a microwave drive, we demonstrate the possibility of achieving an intrinsic average fidelity of 99.8% with experimentally accessible parameters. The gate error can be substantially reduced by increasing the ramp time, suggesting the potential for further improving the gate fidelity and saving gate time. We also investigate the influence of qutrit decoherence on gate performance and find that relaxation times of 100 μs can effectively suppress the gate error to below 0.01. Additionally, through numerical simulations with Gaussian pulses, we further demonstrate the gate operation with perfect population swap between the different excited states $|20\rangle$ and $|01\rangle$. Furthermore, the versatility of the presented gate scheme extends to $\Lambda$ type (or other types) of superconducting qutrits with different anharmonicities. We expect that the application of this protocol to scenarios involving multiple qutrits and diverse excited states will facilitate the construction and simplification of complex superconducting quantum computing architectures.

## APPENDIX A: TOTAL EVOLUTION PATHS AND COUPLING STRENGTH

As mentioned in the main text, according to the fourth-order perturbation theory, there exist 12 evolution paths connecting the states $|200\rangle$ and $|020\rangle$, facilitated by intermediate states $|001\rangle$, $|111\rangle$ and $|110\rangle$. For the intermediate state $|001\rangle$, the four paths are

$$|20011\rangle \leftrightarrow |10111\rangle \leftrightarrow |00121\rangle \leftrightarrow |01021\rangle \leftrightarrow |02020\rangle,$$
$$|20011\rangle \leftrightarrow |10111\rangle \leftrightarrow |00121\rangle \leftrightarrow |01120\rangle \leftrightarrow |02020\rangle,$$
$$|20011\rangle \leftrightarrow |10021\rangle \leftrightarrow |00121\rangle \leftrightarrow |01120\rangle \leftrightarrow |02020\rangle,$$
$$|20011\rangle \leftrightarrow |10021\rangle \leftrightarrow |00121\rangle \leftrightarrow |01021\rangle \leftrightarrow |02020\rangle,$$

$$(A1)$$

for state $|111\rangle$, the paths are

$$|20011\rangle \leftrightarrow |10111\rangle \leftrightarrow |11110\rangle \leftrightarrow |01120\rangle \leftrightarrow |02020\rangle,$$
$$|20011\rangle \leftrightarrow |10111\rangle \leftrightarrow |11110\rangle \leftrightarrow |12010\rangle \leftrightarrow |02020\rangle,$$
$$|20011\rangle \leftrightarrow |21010\rangle \leftrightarrow |11110\rangle \leftrightarrow |12010\rangle \leftrightarrow |02020\rangle,$$
$$|20011\rangle \leftrightarrow |21010\rangle \leftrightarrow |11110\rangle \leftrightarrow |01120\rangle \leftrightarrow |02020\rangle,$$

$$(A2)$$

and for state $|110\rangle$, the paths are

$$|20011\rangle \leftrightarrow |10111\rangle \leftrightarrow |11011\rangle \leftrightarrow |01021\rangle \leftrightarrow |02020\rangle,$$
$$|20011\rangle \leftrightarrow |10111\rangle \leftrightarrow |11011\rangle \leftrightarrow |12010\rangle \leftrightarrow |02020\rangle,$$
$$|20011\rangle \leftrightarrow |10021\rangle \leftrightarrow |11020\rangle \leftrightarrow |01120\rangle \leftrightarrow |02020\rangle,$$
$$|20011\rangle \leftrightarrow |21010\rangle \leftrightarrow |11020\rangle \leftrightarrow |01120\rangle \leftrightarrow |02020\rangle.$$

$$(A3)$$

Here, the notation $|SQ_1, SQ_2, SR, M_1, M_2\rangle$ which denotes the states of qutrit-1, qutrit-2, the resonator, and two drive modes applied to qutrit-1 and qutrit-2, respectively [47]. Accordingly, the above transition paths give rise to the effective coupling between states $|200\rangle$, $|020\rangle$ with the strength $J$ [66]

$$
\begin{aligned}
J = {} & \frac{\sqrt{2}g_1\sqrt{2}\Omega_1 g_2\sqrt{2}\Omega_2}{4(\omega_r - \omega_1 - \alpha_1)\Delta_1'(\omega_2 - \omega_r + \Delta_2')} + \frac{\sqrt{2}g_1\sqrt{2}\Omega_1\Omega_2\sqrt{2}g_2}{4(\omega_r - \omega_1 - \alpha_1)\Delta_1'(\omega_r - \omega_2 - \alpha_2)} + \frac{2\Omega_1 g_1\Omega_2\sqrt{2}g_2}{4(\omega_1 - \omega_r + \Delta_1')\Delta_1'(\omega_r - \omega_2 - \alpha_2)} \\
& + \frac{2\Omega_1 g_1 g_2\sqrt{2}\Omega_2}{4(\omega_1 - \omega_r + \Delta_1')\Delta_1'(\omega_2 - \omega_r + \Delta_1')} + \frac{\sqrt{2}g_1\Omega_2\sqrt{2}\Omega_1\sqrt{2}g_2}{4(\omega_r - \omega_1 - \alpha_1)(\omega_2 + \Delta_1 - \alpha_1 - \omega_2^d)(\omega_r - \omega_2 - \alpha_2)} \\
& + \frac{\sqrt{2}g_1\Omega_2\sqrt{2}g_2\sqrt{2}\Omega_1}{4(\omega_r - \omega_1 - \alpha_1)(\omega_2 + \Delta_1 - \alpha_1 - \omega_2^d)(\omega_1 - \omega_1^d)} + \frac{\Omega_2\sqrt{2}g_1\sqrt{2}g_2\sqrt{2}\Omega_1}{4(\omega_2 - \omega_2^d)(\omega_2 + \Delta_1 - \alpha_1 - \omega_2^d)(\omega_1 - \omega_1^d)} \\
& + \frac{\Omega_2\sqrt{2}g_1\sqrt{2}\Omega_1\sqrt{2}g_2}{4(\omega_2 - \omega_2^d)(\omega_2 + \Delta_1 - \alpha_1 - \omega_2^d)(\omega_r - \omega_2 - \alpha_2)} + \frac{\sqrt{2}g_1 g_2\sqrt{2}\Omega_1\sqrt{2}\Omega_2}{4(\omega_r - \omega_1 - \alpha_1)(\omega_2 - \omega_1 - \alpha_1)(\omega_2 - \omega_r + \Delta_1')} \\
& + \frac{\sqrt{2}g_1 g_2\sqrt{2}\Omega_2\sqrt{2}\Omega_1}{4(\omega_r - \omega_1 - \alpha_1)(\omega_2 - \omega_1 - \alpha_1)(\omega_1 - \omega_1^d)} + \frac{2\Omega_1\Omega_2 g_1\sqrt{2}g_2}{4(\omega_1 - \omega_r + \Delta_1')(\omega_1 - \omega_2 - \alpha_2)(\omega_r - \omega_2 - \alpha_2)} \\
& + \frac{\Omega_2 2\Omega_1 g_1\sqrt{2}g_2}{4(\omega_2 - \omega_2^d)(2\omega_1 - \omega_2 - \alpha_2)(\omega_r - \omega_2 - \alpha_2)},
\end{aligned}
$$

$$(A4)$$

where $\Delta_j = \omega_r - \omega_j$ is the detuning between resonator and qutrit-$j$, $\omega_j^d$ is the frequency of driving mode applied to the qutrit-$j$.

## APPENDIX B: $i$SWAP-LIKE GATE FOR THE THREE-QUTRIT CASE

In this Appendix, we give an analysis of the two-qutrit $i$SWAP-like gate for three qutrits model and demonstrate that a high-fidelity two-qutrit $i$SWAP-like gate can be achieved. Particularly, the proposed gate scheme is useful for realizing arbitrary two-qutrit $i$SWAP-like gates with multiple qutrits coupled to the single resonator which could significantly enhance the scalability of superconducting quantum computing.

The proposed gate scheme can be extended to the case of multiple qutrits. As an example, we consider the case of three qutrits ($SQ_{1,2,3}$) and discuss the $i$SWAP-like gate between the states $|2000\rangle$ and $|0200\rangle$. Here, the state $|2000\rangle$ represents the first qutrit $SQ_1$ in the state $|2\rangle$, both $SQ_2$ and $SQ_3$ in the state $|0\rangle$, with the $SR$ in state $|0\rangle$. Similarly, the quantum state $|0200\rangle$ denotes the $SQ_1$ in the $|0\rangle$ state, $SQ_2$ in the $|2\rangle$, $SQ_3$ in the state $|0\rangle$ and the $SR$ in state $|0\rangle$. By controlling the driven pulses performed on the target qutrits, the proposed gate scheme can be generalized to the three-qutrit case, allowing for high-fidelity $i$SWAP-like gates between any two qutrits. During the implementation of the gate, only two microwave pulses are applied to drive the related qutrits. Assuming that the lowest-energy frequencies for the three qutrits are $w_1/2\pi = 4.5$ GHz, $w_2/2\pi = 6.1$ GHz, and $w_3/2\pi = 6.9$ GHz, with the same anharmonicity $\alpha_{(1,2,3)}/2\pi = -0.3$ GHz and the resonator frequency is $w_r/2\pi = 5.3$ GHz, the coupling
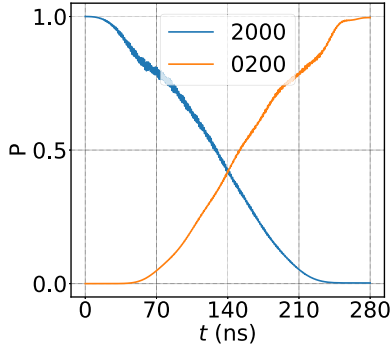
FIG. 7. The *i*SWAP-like gate for the three-qutrit case. The evolution of $|2000\rangle \rightarrow |0200\rangle$ for the multiqutrit case during the gate operation. The microwave pulse parameters are choosen as follows: $\Omega_{1(2)}/2\pi = 200$ ns, $\delta_{1(2)} = 29$ ns, $t_{r_{1(2)}} = 2.1\delta$, $t_{p_{1(2)}} = 280$ ns, $\omega_1^d/2\pi \simeq 3.353$ GHz, and $\omega_2^d/2\pi \simeq 6.592$ GHz. For further details on the qutrits and resonator parameter values, please refer to Appendix B.

strength between the three qutrits and resonator is fixed at $g_{(1,2,3)}/2\pi = 80$ MHz. The qutrits-resonator detuning is set as $\Delta'_{1(2)}/2\pi = 40$ MHz, and the pulse amplitude is fixed at $\Omega_{1(2)}/2\pi = 200$ MHz.

After analyzing the data, we can calculate the pulse frequency $\omega_1^d/2\pi \simeq 3.353$ GHz. To determine the exact frequency value of $\omega_2^d$ and the gate operation time, we conducted a parameter scan to identify the minimal and maximal populations of the initial and target states. We found that the optimal parameters for complete population swap between states $|2000\rangle$ and $|0200\rangle$ are approximately $\omega_2^d/2\pi \simeq 6.592$ GHz and $t_p \simeq 280$ ns. With these chosen parameters, we investigated the dynamics during the gate operation, as shown in Fig. 7. Using Eq. (10), we calculated that the *i*SWAP-like gate fidelity is $F = 99.74\%$, with single-qubit phases $\varphi_1 \simeq 2.140$ rad, $\varphi_2 \simeq 0.174$ rad, $\varphi_3 \simeq 0.920$ rad, and conditional phase $\phi \simeq 1.372$ rad. Compared to the isolated two qutrits case [see Fig. 4(b)], the value of the driven microwave pulse frequency $\omega_2^d$ required to implement the *i*SWAP-like gate has been slightly affected by the third qutrit. However, using the presented method, it is still possible to determine the good pulse parameter values and achieve a high-fidelity *i*SWAP-like gate for the multiqutrit case.

## APPENDIX C: ANALYSIS OF LEAKAGE ERRORS BASED ON FLOQUET THEORY

As mentioned in the main text, reducing the ramp time can lead to an increase in leakage, potentially compromising gate fidelity. In this study, both the qutrits and resonator have been truncated to four levels, resulting in a 64-dimensional complete state space for the system with $d_1 = 4$ and $d_2 = 60$. The presence of two driving pulses applied to the qutrits adds complexity to analyzing the system dynamics. To simplify the analysis, we employed the rotating wave approximation (RWA). Additionally, we chose a rotating coordinate system with the driving pulse frequency $\omega_1^d$, allowing us to condense the two time-dependent drives into a single one.

Consequently, the following Hamiltonian is obtained:

$$H_F(t) = \sum_j \left[ (w_j - \omega_1^d) q_j^\dagger q_j + \frac{\alpha_j}{2} q_j^\dagger q_j^\dagger q_j q_j \right] + (w_r - \omega_1^d) c^\dagger c$$

$$+ \sum_j g_j (q_j^\dagger c + q_j c^\dagger) + \frac{\Omega_1}{2} (q_1^\dagger + q_1)$$

$$+ \frac{\Omega_2}{2} (e^{-i\Delta'_d t} q_2^\dagger + e^{i\Delta'_d t} q_2), \tag{C1}$$

where $\Delta'_d = \omega_2^d - \omega_1^d$. To identify the leakage states more accurately, we employ the Floquet theory [67,68], which enables us to obtain the eigenstates of $H_F(t)$, commonly referred to as Floquet states [69–72]. Given the periodic nature of the driving pulse, we can express the Hamiltonian $H_F(t)$ as $H_F(t + 2\pi/\Delta'_d)$ [72]. Consequently, we solve for the eigenstates using the following procedure:

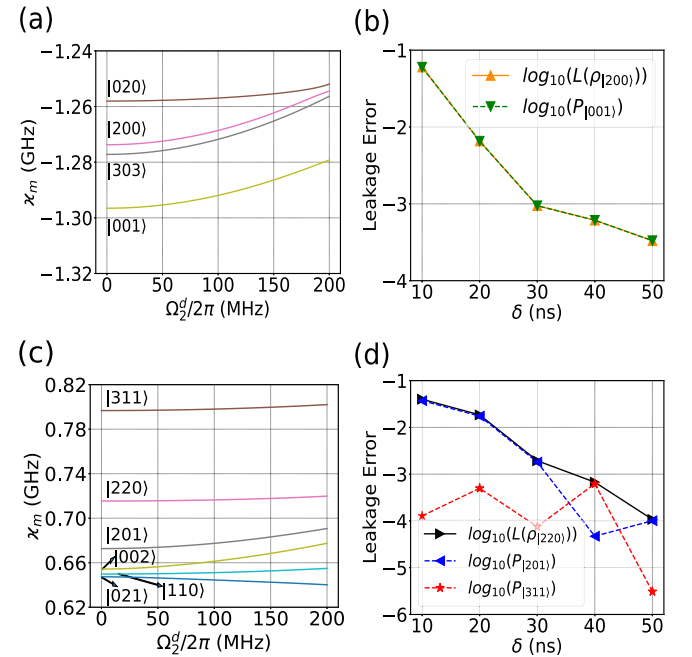$$[H_F(t) - i\partial_t]|\phi_m(t)\rangle = \varkappa_m |\phi_m(t)\rangle. \tag{C2}$$



FIG. 8. Numerical calculations of quasienergies from the Floquet theory and leakage errors after the gate operation. (a) The quasienergies in descending order correspond to the states $|020\rangle$, $|200\rangle$, $|303\rangle$, and $|001\rangle$. (b) Leakage errors originating from state $|200\rangle$ were evaluated for various ramp times. The solid-dark orange line (marked with an up triangle) represents leakage to the noncomputational space, while the dashed-green line (marked with a down triangle) represents leakage to state $|001\rangle$. These results confirm that the main sources of leakage errors for states $|200\rangle$ arise from the interaction between $|200\rangle$ and $|001\rangle$. (c) The quasienergies of the states $\{|311\rangle, |220\rangle, |201\rangle, |002\rangle, |110\rangle, |021\rangle\}$ provide insights into the locations of potential crossings. (d) Numerical results for the leakage errors originating from state $|220\rangle$ for different ramp times. The solid-black line with a right triangle marker represents leakage to the noncomputational space, while the dashed-blue (left triangle marker) and dashed-red (star marker) lines correspond to leakage to states $|201\rangle$ and $|311\rangle$, respectively.

The solutions to Eq. (B2) yield quasienergies $\varkappa_m$, accompanied by corresponding eigenvectors representing the Floquet modes, with $m$ ranging from 1 to 64. It is important to note that the solutions in Eq. (B2) are defined within an integer multiple $k$ of the drive frequency $\Delta'_d$. In other words, if $\{\varkappa_m, |\phi_m(t)\rangle\}$ is a valid solution, then $\{\varkappa_{mk} \equiv \varkappa_m + k\Delta'_d, |\phi_{mk}(t)\rangle = e^{-i\Delta'_d t}|\phi_m(t)\rangle\}$ is also a solution, as a direct consequence of the periodicity exhibited by the Floquet modes.

This study focuses on the main leakage from states $|200\rangle$ (or $|020\rangle$) and $|220\rangle$. Employing the Floquet theory, we are able to determine the quasienergies of the states $|200\rangle$ (or $|020\rangle$) and $|220\rangle$ and their neighboring states that are prone to interaction, as illustrated in Figs. 8(a) and 8(c). By leveraging the relation $\varkappa_{mk} \equiv \varkappa_m + k\Delta'_d$, we can make a rough assessment of the other states in proximity to $|200\rangle$ and $|220\rangle$. As depicted in Fig. 8(a), the quasienergies of the states indicate that the primary sources of leakage errors are the interactions between $|200\rangle$ and $|303\rangle$, as well as $|200\rangle$ and $|001\rangle$. To confirm these leakage occurrences, we conducted numerical calculations to determine the leakage from state $|200\rangle$ to the noncomputational space and the leakage to the state $|001\rangle$ after the gate operation. As shown in Fig. 8(b), the solid-dark orange line (with an up triangle marker) represents leakage to the noncomputational space, while the dashed-green line (marked by a down triangle marker) indicates leakage to the state $|001\rangle$. We can find that the leakage predominantly occurs due to the interaction between $|200\rangle$ and $|001\rangle$, and, by extending the ramp time, the leakage errors can be suppressed heavily. As shown in Fig. 8(a), the main physics behind this is that during the gate operations, the qubit system will sweep through or approach multiple avoid-crossings. The nonadiabatic transitions, i.e., leakages, can be suppressed by slowing down the sweep speed according to the Landau-Zener transitions theory [73]. Additionally, Fig. 8(a) provides evidence that the leakage from the $|020\rangle$ state primarily occurs through the interaction

between $|020\rangle$ and $|001\rangle$. As shown in Fig. 8(a), though the states $|200\rangle$ and $|303\rangle$ are very close, the transition between them is a high-order multiphoton process, resulting in a very weak coupling between them. By contrast, the transition between states $|200\rangle$ and $|001\rangle$ results from a second-order process, giving a large (transition rate) coupling. Thus, here, the leakage mainly happens to state $|001\rangle$, rather than $|303\rangle$.

Next, we examine the leakage errors for the qubit system initialized in the state $|220\rangle$. Using the Floquet theory, we obtained the quasienergies for state $|220\rangle$ and its surrounding states $\{|311\rangle, |201\rangle, |002\rangle, |110\rangle, |021\rangle\}$, as depicted in Fig. 8(c). To determine the main leakage from the $|220\rangle$ state, we numerically calculated the leakage errors to the noncomputational space and the primary states shown in Fig. 8(c). As illustrated in Fig. 8(d), the solid-black line with a right triangle marker represents the errors associated with leakage to the noncomputational space, while the dashed-blue (left triangle marker) and dashed-red (star marker) lines correspond to the errors resulting from leakage to states $|201\rangle$ and $|311\rangle$, respectively. The dashed-blue line demonstrates that the primary leakage state is $|201\rangle$ (while for a ramp time of $\delta = 40$ ns, the dominant leakage state is $|311\rangle$).

Note that, from Fig. 8(d), one can find that the primary leakage source changes with varied ramp times, especially for the ramp time of $\delta = 40$ ns. This can be explained by the following two facts: (1) As shown in Fig. 8(c), during the gate operations, the system will sweep through or approach multiple avoided crossings (due to couplings among qubit states, such as the interactions $|220\rangle \rightarrow |201\rangle$ and $|220\rangle \rightarrow |311\rangle$); (2) for a given avoided crossing, by extending the ramp times, the nonadiabatic transition can be suppressed, thus mitigating the associated leakage. Overall, during the gate operations, the adiabatic conditions for all these avoided crossings cannot be satisfied at the same time for a given ramp time. Thus, for the different ramp times, the dominant leakage channel can be different.

[1] M. Nielsen and I. Chuang, *Quantum Computation and Quantum Information* (Cambridge University Press, Cambridge, England, 2016).

[2] T. D. Ladd, F. Jelezko, R. Laflamme, Y. Nakamura, C. Monroe and J. L. OBrien, Nature (London) **464**, 45 (2010).

[3] F. Arute *et al.*, Nature (London) **574**, 505 (2019).

[4] C. Song *et al.*, Science **365**, 574 (2019).

[5] M. Gong *et al.*, Science **372**, 948 (2021).

[6] A. Barenco, C. H. Bennett, R. Cleve, D. P. Di Vincenzo, N. Margolus, P. Shor, T. Sleator, J. A. Smolin, and H. Weinfurter, Phys. Rev. A **52**, 3457 (1995).

[7] J. Koch, T. M. Yu, J. Gambetta, A. A. Houck, D. I. Schuster, J. Majer, A. Blais, M. H. Devoret, S. M. Girvin, and R. J. Schoelkopf, Phys. Rev. A **76**, 042319 (2007).

[8] J. A. Schreier, A. A. Houck, J. Koch, D. I. Schuster, B. R. Johnson, J. M. Chow, J. M. Gambetta, J. Majer, L. Frunzio, M. H. Devoret, S. M. Girvin, and R. J. Schoelkopf, Phys. Rev. B **77**, 180502(R) (2008).

[9] J. M. Chow, J. M. Gambetta, L. Tornberg, J. Koch, L. S. Bishop, A. A. Houck, B. R. Johnson, L. Frunzio, S. M. Girvin, and R. J. Schoelkopf, Phys. Rev. Lett. **102**, 090502 (2009).

[10] J. M. Chow, L. DiCarlo, J. M. Gambetta, F. Motzoi, L. Frunzio, S. M. Girvin, and R. J. Schoelkopf, Phys. Rev. A **82**, 040305(R) (2010).

[11] N. Leung, M. Abdelhafez, J. Koch, and D. Schuster, Phys. Rev. A **95**, 042318 (2017).

[12] M. Abdelhafez, D. I. Schuster, and J. Koch, Phys. Rev. A **99**, 052327 (2019).

[13] P. Krantz, M. Kjaergaard, F. Yan, T. P. Orlando, S. Gustavsson, and W. D. Oliver, Appl. Phys. Rev. **6**, 021318 (2019).

[14] A. Blais, A. L. Grimsmo, S. M. Girvin, and A. Wallraff, Rev. Mod. Phys. **93**, 025005 (2021).

[15] E. T. Campbell, H. Anwar, and D. E. Browne, Phys. Rev. X **2**, 041021 (2012).

[16] E. T. Campbell, Phys. Rev. Lett. **113**, 230501 (2014).

[17] H. Anwar, B. J. Brown, E. T. Campbell, and D. E. Browne, New J. Phys. **16**, 063038 (2014).

[18] A. Krishna and J. P. Tillich, Phys. Rev. Lett. **123**, 070507 (2019).

[19] D. Bruß and C. Macchiavello, Phys. Rev. Lett. **88**, 127901 (2002).

[20] H. Bechmann-Pasquinucci and A. Peres, Phys. Rev. Lett. **85**, 3313 (2000).

[21] M. Neeley, M. Ansmann, C. Radoslaw, M. Bialczak, M. Hofheinz, E. Lucero, A. D. O'Connell, D. Sank, H. Wang, J. Wenner, A. N. Cleland, M. R. Geller, and J. M. Martinis, Science **325**, 722 (2009).

[22] M. Kues, C. Reimer, P. Roztocki, L. Romero Cortés, S. Sciara, B. Wetzel, Y. Zhang, A. Cino, S. T. Chu, B. E. Little, D. J. Moss, L. Caspani, J. Azaña, and R. Morandotti, Nature (London) **546**, 622 (2017).

[23] Y. Wang, Z. X. Hu, B. C. Sanders, and S. Kais, Front. Phys. **8**, 589504 (2020).

[24] P. Gokhale, J. M. Baker, C. Duckering, F. T. Chong, N. C. Brown, and K. R. Brown, IEEE Micro **40**, 64 (2020).

[25] M. S. Blok, V. V. Ramasesh, T. Schuster, K. OBrien, J. M. Kreikebaum, D. Dahlen, A. Morvan, B. Yoshida, N. Y. Yao, and I. Siddiqi, Phys. Rev. X **11**, 021010 (2021).

[26] P. Liu, R. Wang, J.-N. Zhang, Y. Zhang, X. Cai, H. Xu, Z. Li, J. Han, X. Li, G. Xue, W. Liu, L. You, Y. Jin, and H. Yu, Phys. Rev. X **13**, 021028 (2023).

[27] F. Mallet, F. R. Ong, A. Palacios-Laloy, F. Nguyen, P. Bertet, D. Vion, and D. Esteve, Nat. Phys. **5**, 791 (2009).

[28] P. Jurcevic, A. Javadi-Abhari, L. S. Bishop *et al.*, Quantum Sci. Technol. **6**, 025020 (2021).

[29] A. R. Shlyakhov, V. V. Zemlyanov, M. V. Suslov, A. V. Lebedev, G. S. Paraoanu, G. B. Lesovik, and G. Blatter, Phys. Rev. A **97**, 022115 (2018).

[30] A. Cervera-Lierta, M. Krenn, A. Aspuru-Guzik, and A. Galda, Phys. Rev. Appl. **17**, 024062 (2022).

[31] A. Galda *et al.*, arXiv:2109.00558.

[32] T. Bækkegaard, L. B. Kristensen, N. J. S. Loft, C. K. Andersen, D. Petrosyan, and N. T. Zinner, Sci. Rep. **9**, 13389 (2019).

[33] J. M. Baker, C. Duckering, P. Gokhale, N. C. Brown, K. R. Brown, and F. T. Chong, ACM Trans. Quantum Comput. **1**, 1 (2020).

[34] A. S. Nikolaeva, E. O. Kiktenko, and A. K. Fedorov, Phys. Rev. A **105**, 032621 (2022).

[35] T. C. Ralph, K. J. Resch, and A. Gilchrist, Phys. Rev. A **75**, 022313 (2007).

[36] R. Barends *et al.*, Nature (London) **508**, 500 (2014).

[37] Y. Chen, C. Neill, P. Roushan, N. Leung, M. Fang, R. Barends, J. Kelly, B. Campbell, Z. Chen, B. Chiaro *et al.*, Phys. Rev. Lett. **113**, 220502 (2014).

[38] M. C. Collodo, J. Herrmann, N. Lacroix, C. K. Andersen, A. Remm, S. Lazar, J.-C. Besse, T. Walter, A. Wallraff, and C. Eichler, Phys. Rev. Lett. **125**, 240502 (2020).

[39] B. Foxen *et al.*, Phys. Rev. Lett. **125**, 120504 (2020).

[40] V. Negîrneac, H. Ali, N. Muthusubramanian, F. Battistel, R. Sagastizabal, M. S. Moreira, J. F. Marques, W. Vlothuizen, M. Beekman, N. Haider, A. Bruno, and L. Dicarlo, Phys. Rev. Lett. **126**, 220502 (2021).

[41] Y. Sung, L. Ding, J. Braumüller, A. Vepsäläinen, B. Kannan, M. Kjaergaard, A. Greene, G. O. Samach, C. Mcnally, D. Kim, A. Melville, B. M. Niedzielski, M. E. Schwartz, J. L. Yoder, T. P. Orlando, S. Gustavsson, and W. D. Oliver, Phys. Rev. X **11**, 021058 (2021).

[42] L. DiCarlo, J. M. Chow, J. M. Gambetta, L. S. Bishop, B. R. Johnson, D. I. Schuster, J. Majer, A. Blais, L. Frunzio, S. M. Girvin, and R. J. Schoelkopf, Nature (London) **460**, 240 (2009).

[43] R. C. Bialczak, M. Ansmann, M. Hofheinz, E. Lucero, M. Neeley, A. D. O'Connell, D. Sank, H. Wang, J. Wenner, M. Steffen, A. N. Cleland, and J. M. Martinis, Nat. Phys. **6**, 409 (2010).

[44] A. Blais, R.-S. Huang, A. Wallraff, S. M. Girvin, and R. J. Schoelkopf, Phys. Rev. A **69**, 062320 (2004).

[45] A. Blais, J. Gambetta, A. Wallraff, D. I. Schuster, S. M. Girvin, M. H. Devoret, and R. J. Schoelkopf, Phys. Rev. A **75**, 032329 (2007).

[46] J. Majer, J. M. Chow *et al.*, Nature (London) **449**, 443 (2007).

[47] P. Zhao, X. Tan, H. Yu, S.-L. Zhu, and Y. Yu, Phys. Rev. A **95**, 063848 (2017).

[48] S. Zeytinoğlu, M. Pechal, S. Berger, A. A. Abdumalikov, A. Wallraff, and S. Filipp, Phys. Rev. A **91**, 043846 (2015).

[49] D. J. Egger, M. Ganzhorn, G. Salis, A. Fuhrer, P. Muller, P. K. Barkoutsos, N. Moll, I. Tavernelli, and S. Filipp, Phys. Rev. Appl. **11**, 014017 (2019).

[50] J. Ghosh, A. Galiautdinov, Z. Zhou, A. N. Korotkov, J. M. Martinis, and M. R. Geller, Phys. Rev. A **87**, 022309 (2013).

[51] R. Barends, C. M. Quintana, A. G. Petukhov, Y. Chen, D. Kafri, K. Kechedzhi, R. Collins, O. Naaman, S. Boixo, F. Arute *et al.*, Phys. Rev. Lett. **123**, 210501 (2019).

[52] L. H. Pedersen, N. M. Møller, and K. Mølmer, Phys. Lett. A **367**, 47 (2007).

[53] E. Zahedinejad, J. Ghosh, and B. C. Sanders, Phys. Rev. Appl. **6**, 054005 (2016).

[54] E. Barnes, C. Arenz, A. Pitchford, and S. E. Economou, Phys. Rev. B **96**, 024504 (2017).

[55] P. Zhao, P. Xu, D. Lan, X. Tan, H. Yu, and Y. Yu, Phys. Rev. Appl. **14**, 064016 (2020).

[56] M. Malekakhlagh and E. Magesan, Phys. Rev. A **105**, 012602 (2022).

[57] V. Tripathi, M. Khezri, and A. N. Korotkov, Phys. Rev. A **100**, 012301 (2019).

[58] K. X. Wei, E. Pritchett, D. M. Zajac, D. C. McKay, and S. Merkel, arXiv:2302.10881.

[59] C. J. Wood and J. M. Gambetta, Phys. Rev. A **97**, 032306 (2018).

[60] A. Megrant, C. Neill, R. Barends, B. Chiaro, Y. Chen, L. Feigl, J. Kelly, E. Lucero, M. Mariantoni, P. J. J. O'Malley *et al.*, Appl. Phys. Lett. **100**, 113510 (2012).

[61] G. Calusine, A. Melville, W. Woods, R. Das, C. Stull, V. Bolkhovsky, D. Braje, D. Hover, D. K. Kim, X. Miloshi *et al.*, Appl. Phys. Lett. **112**, 062601 (2018).

[62] R. Gao, W. Yu, H. Deng, H.-S. Ku, Z. Li, M. Wang, X. Miao, Y. Lin, and C. Deng, Phys. Rev. Mater. **6**, 036202 (2022).

[63] H. J. Carmichael, *Statistical Methods in Quantum Optics 1: Master Equations and Fokker-Planck Equations*, 2nd ed., (Springer, New York, 2002).

[64] A. P. M. Place, L. V. H. Rodgers, P. Mundada, B. M. Smitham, M. Fitzpatrick, Z. Leng, A. Premkumar, J. Bryon, S. Sussman, G. Cheng *et al.*, Nat. Commun. **12**, 1779 (2021).

[65] C. Wang, X. Li, H. Xu *et al.*, npj Quantum Inf. **8**, 3 (2022).

[66] A. F. Kockum, A. Miranowicz, V. Macrì, S. Savasta, and F. Nori, Phys. Rev. A **95**, 063849 (2017).

[67] A. Petrescu, C. Le Calonnec, C. Leroux, A. Di Paolo, P. Mundada, S. Sussman, A. Vrajitoarea, A. A. Houck, and A. Blais, Phys. Rev. Appl. **19**, 044003 (2023).

[68] Y. Zhang, B. J. Lester, Y. Y. Gao, L. Jiang, R. J. Schoelkopf, and S. M. Girvin, Phys. Rev. A **99**, 012314 (2019).

[69] J. H. Shirley, Phys. Rev. **138**, B979 (1965).

[70] Y. B. Zel'Dovich, Sov. Phys. JETP **24**, 1006 (1967).

[71] V. I. Ritus, Sov. Phys. JETP **24**, 1041 (1967).

[72] H. Sambe, Phys. Rev. A **7**, 2203 (1973).

[73] O. V. Ivakhnenko, S. N. Shevchenko, and F. Nori, Phys. Rep. **995**, 1 (2023).